

Customized data-driven RANS closures for bi-fidelity LES–RANS optimization

Zhang, Yu; Dwight, Richard P.; Schmelzer, Martin; Gómez, Javier F.; Han, Zhong hua; Hickel, Stefan

DOI

[10.1016/j.jcp.2021.110153](https://doi.org/10.1016/j.jcp.2021.110153)

Publication date

2021

Document Version

Final published version

Published in

Journal of Computational Physics

Citation (APA)

Zhang, Y., Dwight, R. P., Schmelzer, M., Gómez, J. F., Han, Z. H., & Hickel, S. (2021). Customized data-driven RANS closures for bi-fidelity LES–RANS optimization. *Journal of Computational Physics*, 432, Article 110153. <https://doi.org/10.1016/j.jcp.2021.110153>

Important note

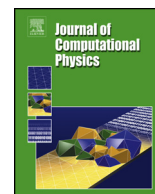
To cite this publication, please use the final published version (if applicable). Please check the document version above.

Copyright

Other than for strictly personal use, it is not permitted to download, forward or distribute the text or part of it, without the consent of the author(s) and/or copyright holder(s), unless the work is under an open content license such as Creative Commons.

Takedown policy

Please contact us and provide details if you believe this document breaches copyrights. We will remove access to the work immediately and investigate your claim.



Customized data-driven RANS closures for bi-fidelity LES–RANS optimization [☆]

Yu Zhang ^a, Richard P. Dwight ^{b,*}, Martin Schmelzer ^b, Javier F. Gómez ^b,
Zhong-hua Han ^a, Stefan Hickel ^b

^a Institute of Aerodynamic and Multidisciplinary Design Optimization, National Key Laboratory of Science and Technology on Aerodynamic Design and Research, School of Aeronautics, Northwestern Polytechnical University, Youyi West Road 127, 710072 Xi'an, People's Republic of China

^b Aerodynamics Group, Faculty of Aerospace Engineering, Delft University of Technology, Kluyverweg 2, 2629 HS Delft, the Netherlands



ARTICLE INFO

Article history:

Received 6 April 2020

Received in revised form 18 September 2020

Accepted 8 December 2020

Available online 26 January 2021

Keywords:

Turbulence modelling

Algebraic stress model

Reynolds-averaged Navier-Stokes

Large-eddy simulation

Multi-fidelity optimization

ABSTRACT

Multi-fidelity optimization methods promise a high-fidelity optimum at a cost only slightly greater than a low-fidelity optimization. This promise is seldom achieved in practice, due to the requirement that low- and high-fidelity models correlate well. In this article, we propose an efficient bi-fidelity shape optimization method for turbulent fluid-flow applications with Large-Eddy Simulation (LES) and Reynolds-averaged Navier–Stokes (RANS) as the high- and low-fidelity models within a hierarchical-Kriging surrogate modelling framework. Since the LES–RANS correlation is often poor, we use the full LES flow-field at a single point in the design space to derive a *custom-tailored RANS closure model* that reproduces the LES at that point. This is achieved with machine-learning techniques, specifically sparse regression to obtain high corrections of the turbulence anisotropy tensor and the production of turbulence kinetic energy as functions of the RANS mean-flow. The LES–RANS correlation is dramatically improved throughout the design-space. We demonstrate the effectivity and efficiency of our method in a proof-of-concept shape optimization of the well-known periodic-hill case. Standard RANS models perform poorly in this case, whereas our method converges to the LES-optimum with only two LES samples.

© 2021 The Author(s). Published by Elsevier Inc. This is an open access article under the CC BY license (<http://creativecommons.org/licenses/by/4.0/>).

1. Introduction

Numerical fluid-dynamic shape-optimization is an increasingly central tool in engineering practice. Typically Reynolds-Averaged Navier–Stokes (RANS) is used as the fluid model, due to its acceptable computational cost and accuracy. However in many important situations, the physics demands scale-resolving simulations of turbulence such as large-eddy simulation (LES). This includes, for instance, designs where separation occurs; junctions flows with complex turbulence behavior (Simpson [34], Belligoli et al. [2]); and novel boundary layer flow control applications. LES is often applied for a final analysis and validation, but its high computational cost precludes its use within the design loop.

[☆] This document is the results of the research project funded by Innovation Foundation for Doctor Dissertation of Northwestern Polytechnical University under grant No. CX201801 and China Scholarship Council No. 201706290083.

* Corresponding author.

E-mail addresses: zhangyu91@mail.nwpu.edu.cn (Y. Zhang), r.p.dwight@tudelft.nl (R.P. Dwight), m.schmelzer@tudelft.nl (M. Schmelzer), jfatoug@gmail.com (J.F. Gómez), hazh@nwpu.edu.cn (Z.-h. Han), s.hickel@tudelft.nl (S. Hickel).

<https://doi.org/10.1016/j.jcp.2021.110153>

0021-9991/© 2021 The Author(s). Published by Elsevier Inc. This is an open access article under the CC BY license (<http://creativecommons.org/licenses/by/4.0/>).

Multi-fidelity optimization (MFO) methods are supposed to address exactly this dilemma. In MFO, low-fidelity but cheap-to-evaluate physics models are used to explore the design-space rapidly; their predictions are then corrected by a few expensive high-fidelity simulations. One such class of methods are the multi-fidelity surrogate modelling methods (Han and Görtz [13]), combined with a suitable sampling criteria (Jones et al. [20]).

There has been significant work on multi-fidelity surrogate modelling methods, almost all based on Gaussian-process models for the surrogate (i.e. Kriging), differing mainly in the manner in which the high-fidelity correct the lower. Haftka [10] and Chang et al. [4] developed a variable-fidelity Kriging model using a multiplicative “bridge function” to correct the low-fidelity model. Gano et al. [9] developed a hybrid bridge function method, which uses a second Kriging model to scale the low-fidelity model. Han et al. [14] combined gradient information and a generalized hybrid bridge function. Co-Kriging was originally proposed in the geostatistics community by Journel and Huijbregts [21] and then extended to deterministic computer experiments by Kennedy and O’Hagan [23]. Han et al. [15] proposed an improved version of co-Kriging, which can be built in one step, and a hierarchical Kriging (HK) model (Han and Görtz [13]), appears to be as simple and robust as the correction-based method and as accurate as co-Kriging method.

However, the success of all these approaches relies heavily on the correlation between the high- and low-fidelity models (Han et al. [12], Zhang et al. [39]). Since models with higher fidelity typically have also significantly higher numerical costs, in practice the high-fidelity model is chosen as the cheapest model that predicts the relevant physics. Necessarily, the low-fidelity model will lack some of the relevant physics, leading to a poor correlation between the models, which limits the practical application of MFO methods.

In separate developments of the past few years, data-driven methods for turbulence modelling based on supervised machine learning have been introduced to improve RANS predictions when reference data is available (Xiao and Cinnella [38], Duraisamy et al. [6], Durbin [7], Kaandorp and Dwight [22]). Notably, Parish and Duraisamy [29] introduced a local multiplicative term to correct the turbulence production in the $k-\omega$ model. This term was chosen by solving an inverse problem to match LES reference data, and was then used to train a Gaussian process to correct the baseline turbulence model. Ling et al. [24] trained a deep neural network to predict turbulence anisotropy a_{ij} and replace the baseline turbulence model. An alternative is to use random-forests for the same task (Wang et al. [35], Kaandorp and Dwight [22]). Even though these approaches generalize the linear eddy-viscosity concept, they generate complex black-box closure models. More promising are approaches that generate compact explicit expressions for models. Notable are gene-expression programming (GEP) (Weatheritt and Sandberg [36,37]), and deterministic sparse regression of turbulence anisotropy (SpaRTA) (Schmelzer et al. [33]). These methods generate models that can be rapidly implemented in existing CFD codes and evaluated at every iteration of a RANS solution, and potentially inspected to identify the physical mechanisms influencing the flow. The SpaRTA approach has shown the ability to consistently reproduce specified LES mean-values in a RANS solver, using only three to five additional non-linear closure terms. It is important to understand that – at their present level of development – these methods do not generate general-purpose turbulence models, but rather deliver corrections for flows similar to the flow they were trained on. Thus, for flows with a high degree of similarity, e.g. modifications in the geometry, the methods generate models effectively customized to the flow at hand.

The key original contribution of this paper is a highly-efficient bi-fidelity optimization procedure, using LES as the high-fidelity model, and *data-enhanced* RANS as the low-fidelity model. In outline, we:

1. Perform a single LES simulation at the baseline geometry ψ_0 , $i = 0$;
2. Use the full-field LES data to generate a customized RANS model matching the LES at ψ_i ;
3. Sample this custom RANS model throughout the design-space (cheap);
4. Combine custom-RANS and LES results in a bi-fidelity surrogate;
5. Perform a new LES at the point of maximum expected improvement ψ_{i+1} (expensive);
6. Generate new custom RANS model(s), based on all LES data available so far;
7. $i \leftarrow i + 1$, goto 3.

The key observation is that the custom RANS model correlates well with LES in a region of the design-space for which the LES training data is informative, and that this correlation applies to mean-velocities as well as the Reynolds-stresses (originating from the LES training data). Provided the physical processes occurring do not significantly change, the data-driven RANS remains a viable model. Also, whereas typical multi-fidelity methods use only the objective function from the high-fidelity simulation, our approach uses much more information. There are many variations on the basic pattern described above, for example: Which LES samples are used for training in Step 6?; What criteria are used for sampling RANS in Step 3, and LES in Step 5?.

In the following we demonstrate the method on a proof-of-concept optimization problem: a generalized periodic-hill (P-H) geometry, in which the steepness of the hills is varied (Fatou Gómez [8]). The baseline periodic-hill flow (as proposed by Mellen et al. [25] based on an experimental study by Almeida et al. [1]) is notorious for poor performance of essentially all standard RANS models, due to its sensitivity on the flow separation location and large-scale low-frequency dynamics. We use a hierarchical Kriging bi-fidelity surrogate model, with an *efficient global optimization* (EGO) sampling procedure for the LES (Jones et al. [20], Zhang et al. [39]). The custom RANS model is sampled on a uniform grid, and updated at each step with the latest LES data. To achieve the LES optimal solution we require only two LES samples (and one further sample to

verify the result). Our method therefore offers a promising path towards LES-quality optimization with only a handful of LES samples.

The paper is structured as follows: in Section 2 we describe the computational setting of the baseline RANS and LES simulations. Section 3 briefly describes SpaRTA, the machine-learning method used in this work to generate data-driven RANS models. SpaRTA is demonstrated on the baseline periodic-hill case (Mellen et al. [25]). Our proposed bi-fidelity optimization procedure is described in detail, and applied to the generalized P-H optimization case with the hill width as a design variable in Section 4.

2. Baseline incompressible LES and RANS simulations

The solvers used here for LES and RANS are both finite-volume methods, but otherwise numerically distinct - we describe both briefly. For the standard periodic-hill test-case we compare our LES results with the experimental data of Rapp [32] and well-resolved LES reference data from Breuer et al. [3], and demonstrate excellent agreement. We show that RANS results obtained with a standard k - ω SST model are poor, which is in agreement with literature.

2.1. Baseline Reynolds-averaged Navier-Stokes with k - ω SST

Assuming incompressible flow with constant fluid density equal to unity, the steady RANS equations are

$$\begin{aligned} \frac{\partial U_i}{\partial x_i} &= 0, \\ U_j \frac{\partial U_i}{\partial x_j} &= \frac{\partial}{\partial x_j} \left[-\delta_{ij} P + \nu \frac{\partial U_i}{\partial x_j} - \tau_{ij} \right] + \delta_{i1} f, \end{aligned} \quad (1)$$

where U_i with $i, j \in \{1, 2, 3\}$ are the components of the mean-flow velocity, P is the mean pressure, and ν is the kinematic viscosity. The volume forcing f serves to drive the flow through the doubly periodic domain. The effect of turbulence on the momentum equation is confined to the Reynolds stress tensor τ_{ij} , which must be modelled. In this paper, we use the popular k - ω SST model as a baseline model. The model defines transport equations for the turbulence kinetic energy $k := \frac{1}{2} \tau_{ii}$, and the specific turbulence dissipation rate ω :

$$U_j \frac{\partial k}{\partial x_j} = \underbrace{\tau_{ij} \frac{\partial U_i}{\partial x_j}}_{P_k} - \beta^* k \omega + \frac{\partial}{\partial x_j} \left[(\nu + \sigma_k \nu_t) \frac{\partial k}{\partial x_j} \right], \quad (2)$$

$$U_j \frac{\partial \omega}{\partial x_j} = \frac{\gamma}{\nu_t} \tau_{ij} \frac{\partial U_i}{\partial x_j} - \beta \omega^2 + \frac{\partial}{\partial x_j} \left[(\nu + \sigma_\omega \nu_t) \frac{\partial \omega}{\partial x_j} \right] + 2(1 - F_1) \sigma_{\omega 2} \frac{1}{\omega} \frac{\partial k}{\partial x_j} \frac{\partial \omega}{\partial x_j}. \quad (3)$$

The eddy viscosity is modelled as

$$\nu_t := \frac{a_1 k}{\max(a_1 \omega, S F_2)},$$

and the anisotropic part of Reynolds-stress tensor is modelled by the Boussinesq assumption

$$a_{ij} := \tau_{ij} - \frac{2}{3} \delta_{ij} k \simeq a_{ij}^B := -2\nu_t S_{ij}, \quad \text{where } S_{ij} := \frac{1}{2} \left(\frac{\partial U_i}{\partial x_j} + \frac{\partial U_j}{\partial x_i} \right),$$

and the isotropic part is absorbed into the pressure. All remaining terms and coefficients are omitted for brevity, see (Menter [26]) for details.

The computational mesh used for RANS simulation of the periodic-hill is two-dimensional, with 120×130 cells in stream-wise and wall-normal directions respectively, achieving $y^+ \leq 1$ on all walls. Periodic boundary conditions are set at inlet and outlet, and no-slip conditions on the walls. Volume forcing is used to drive the flow, with a *proportional-integral-derivative* (PID) controller used to achieve the target velocity. The simulation is performed at $Re_h = 10595$ based on the hill height h using second-order accurate SIMPLE solver. The pressure is solved using geometric-algebraic multigrid with a Gauss-Seidel smoother, while U_i , k and ω are solved using a Diagonal-Incomplete-LU-preconditioned BiCG method.

2.2. Large-eddy simulation for the periodic-hills

The high-fidelity and ‘‘ground-truth’’ model in this work is wall-modelled LES with our in-house finite-volume solver INCA. We use the incompressible staggered-grid version of the solver with a block-Cartesian background mesh and the conservative immersed boundary method of Meyer et al. [27] for representing the geometry. Our LES follow a holistic modelling approach, where the numerical discretization and the subgrid-scale (SGS) turbulence closure are fully merged: The adaptive local deconvolution method (ALDM) of Hickel et al. [17], Hickel and Adams [16] is a nonlinear finite-volume

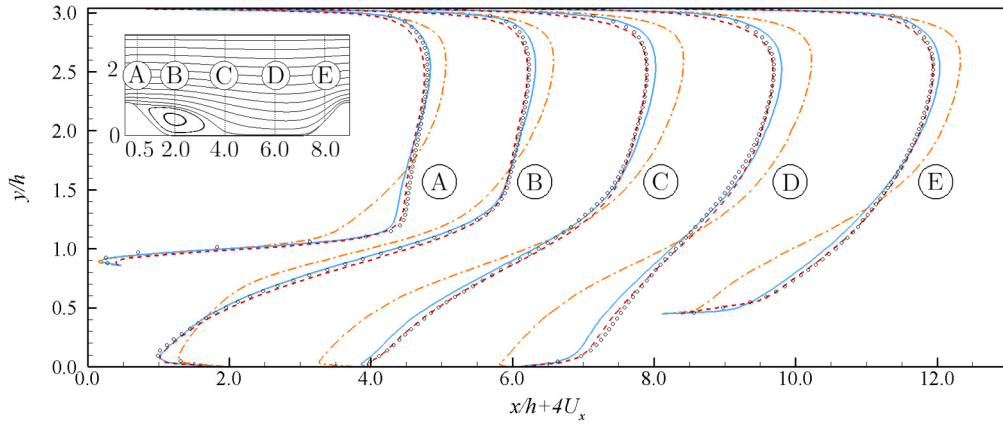


Fig. 1. Mean velocity profiles for: reference LES (—) (Breuer et al. [3]); PIV (○) (Rapp [32]), our LES (---) and RANS with $k-\omega$ SST turbulence modelling (---). (For interpretation of the colors in the figure(s), the reader is referred to the web version of this article.)

discretization scheme tailored for LES of turbulent flows. Optimum model form and discretization parameters were learnt by a physics-informed genetic algorithm using turbulence data, spectral analysis and constraints from turbulence theory (Hickel et al. [17]).

The near-wall turbulence is modelled rather than resolved (Hickel et al. [19]). In particular we use the model of (Chen et al. [5]), based on the turbulence boundary-layer equations and a mixing-length eddy-viscosity model. Validation results for the periodic-hills – amongst other cases – are available in (Chen et al. [5]). At the wall our grids maintain $y^+ < 20$. A third-order explicit Runge-Kutta scheme is used for time integration and the pressure-correction Poisson equation is solved using BiCGstab with incomplete LU and algebraic-multigrid as preconditioners. Overall, our LES solver is very similar to that used by Hickel et al. [18] for wall-resolved LES of the periodic-hill flow, and largely identical to that used by Meyer et al. [28] for wall-modelled LES of a low-speed aerospace application.

The periodic hill is computed with a domain size of $(9h, 3.03h, 4.5h)$ with h = the hill height, the geometry and boundary conditions follow exactly the standard definitions of the ERCOFTAC Testcase 9.2 [25]. A parameter study was performed on the effects of the span-wise extent of the domain, the mesh resolution, and the solution averaging time (Fatou Gómez [8]). A good compromise of accuracy and cost was achieved for a spanwise extent of $L_z = 4.5h$, about 1.2 million cells (giving $y^+ < 20$ everywhere), and averaging over $\simeq 55$ flow-through times started after an initial transient of $\simeq 89$ flow-through times.

The LES simulation code is parallelized by domain decomposition based on the Message Passing Interface (MPI) library, and was run on 20 Intel(R) Xeon(R) CPU E5-2670v2 cores at 2.5 GHz. At these conditions each case cost approximately two days of wall-clock time, with steeper geometries generally more costly than shallow cases.

With these parameters, the simulations are performed on the TU delft HPC, and converged statistics are obtained in less than 2 days on a 20 cores Intel^(R) Xeon^(R) CPU E5-2670v2 at 2.5 GHz and 128 GB of RAM. Fig. 1 shows our LES results for the mean velocity profiles at several streamwise locations for the standard periodic-hill geometry and the well-resolved LES data of Breuer et al. [3] (13.1 million cells) and the reference experiments of Rapp [32]. We observe that our INCA LES results are in very good agreement with the reference data.

Also shown in Fig. 1 are the RANS results for the baseline $k-\omega$ SST model described in Section 2.1. The RANS simulation significantly over-predicts the length of the separated flow region, which distorts the flow and leads to large errors everywhere in the domain. Having flow-features very dissimilar to the high-fidelity LES, the baseline RANS is therefore likely inappropriate as a low-fidelity model in a bi-fidelity optimization or surrogate modelling procedure.

3. Enhancing RANS with data-driven turbulence modelling

In this section we briefly describe the SpARTA procedure to generate improved RANS models from LES data – see [33] for a detailed discussion. The procedure has two main stages:

1. We use the k -corrective-frozen-RANS approach (Schmelzer et al. [33]) to solve for corrective fields for the anisotropy tensor, and turbulence production. These fields, when directly injected into the RANS solver, lead the solver to reproduce the LES mean-flow.
2. We use deterministic symbolic regression to find a low-complexity approximate map from the resolved mean-flow quantities to these corrective fields. This map represents our correction to the baseline turbulence model.

The result is a RANS closure model customized for a particular flow.

3.1. Identifying model-form error with the k -corrective-frozen-RANS approach

It is well known (Xiao and Cinnella [38]) that injecting LES/DNS Reynolds stresses directly into RANS solvers does not always improve accuracy of the mean-flow prediction. This issue can be partially addressed by using a field inversion procedure to identify corrective fields that result in the correct mean-flow (Duraismy et al. [6]). In our problem full-field LES data is available, and so a costly inversion procedure is unnecessary. Instead we define an iteration that leads to equivalent corrective fields.

Let LES statistics be denoted with a superscript “ \star ”, so $b_{ij}^\star = a_{ij}^\star/2k^\star$ is the normalized LES anisotropy tensor, k^\star is the LES turbulence kinetic energy, and U^\star the LES mean velocity field. We define a correction to the normalized anisotropy tensor b_{ij}^Δ via:

$$b_{ij}^\star = b_{ij}^{\star B} + b_{ij}^\Delta, \quad b_{ij}^{\star B} := -\frac{\hat{\nu}_t}{k^\star} S_{ij}^\star, \quad (4)$$

where the correction is defined with respect to the Boussinesq assumption evaluated using the LES strain-rate tensor S_{ij}^\star , k^\star and eddy-viscosity $\hat{\nu}_t$. Parneix et al. [30] and Weatheritt and Sandberg [37] model the specific dissipation rate ω by passively evaluating the ω -equation (3), using LES data for other quantities. We further extend this procedure by requiring that the k equation also satisfies the LES data, the so-called k -corrective-frozen-RANS approach. To this end we introduce a (spatially varying) correction $\hat{\mathbf{R}}$ to the k - and ω -equations giving:

$$U_j^\star \frac{\partial k^\star}{\partial x_j} = P_k^\star + \hat{\mathbf{R}} - \beta^\star k^\star \hat{\omega} + \frac{\partial}{\partial x_j} \left[(v + \sigma_k \hat{\nu}_t) \frac{\partial k^\star}{\partial x_j} \right], \quad (5)$$

$$U_j^\star \frac{\partial \hat{\omega}}{\partial x_j} = \frac{\gamma}{\hat{\nu}_t} (P_k^\star + \hat{\mathbf{R}}) - \beta \hat{\omega}^2 + \frac{\partial}{\partial x_j} \left[(v + \sigma_\omega \hat{\nu}_t) \frac{\partial \hat{\omega}}{\partial x_j} \right] + 2(1 - F_1) \sigma_{\omega 2} \frac{1}{\hat{\omega}} \frac{\partial k^\star}{\partial x_j} \frac{\partial \hat{\omega}}{\partial x_j}, \quad (6)$$

in which quantities with a “ \wedge ” are to be solved for, and remaining quantities derive from the LES data. The LES data is interpolated onto a RANS mesh, (5) and (6) are solved readily in a loosely coupled fashion, and the resulting $\hat{\omega}$ is used to compute b_{ij}^Δ from (4). Thus two corrective fields result, the tensor-field b_{ij}^Δ and the scalar-field $\hat{\mathbf{R}}$. When these fields are injected into the RANS solver, the resulting mean-fields consistently agree well with LES, see Fig. 2. This is true for both the baseline periodic hills with the width $\psi = 1$, and steeper and shallower hills with $0.25 \leq \psi \leq 4$ - i.e. the full design space (Mellen et al. [25]).

3.2. Deterministic symbolic regression for corrective field modelling

Having identified corrective fields, to make predictions it is necessary to model these fields in terms of known (mean-flow) quantities. Following Pope [31], we assume that the non-dimensional strain-rate and rotation-rate tensors

$$\tilde{S}_{ij} := \frac{1}{\omega} S_{ij}, \quad \tilde{\Omega}_{ij} := \frac{1}{2\omega} \left(\frac{\partial U_i}{\partial x_j} - \frac{\partial U_j}{\partial x_i} \right)$$

are sufficient to describe the corrective fields, leading to Pope’s well-known basis-tensor series. The Cayley-Hamilton theorem dictates that the most general form of the function $b_{ij}^\Delta(\tilde{S}_{ij}, \tilde{\Omega}_{ij})$ is (under the assumptions of analyticity and Galilean invariance):

$$b_{ij}^\Delta(\tilde{S}_{ij}, \tilde{\Omega}_{ij}) = \sum_{n=1}^{10} T_{ij}^{(n)} \alpha_n(\lambda_1, \dots, \lambda_5), \quad (7)$$

where $T_{ij}^{(n)}$ are ten basis tensors, λ_m are the five invariants of \tilde{S} and $\tilde{\Omega}$, and $\alpha_n(\cdot)$ are arbitrary scalar functions of these invariants. In this paper, we only consider the first three base tensors, and first two invariants, which are given by:

$$\begin{aligned} T_{ij}^{(1)} &= \tilde{S}_{ij} & \lambda_1 &= \tilde{S}_{mn} \tilde{S}_{nm}, \\ T_{ij}^{(2)} &= \tilde{S}_{ik} \tilde{\Omega}_{kj} - \tilde{\Omega}_{ik} \tilde{S}_{kj} & \lambda_2 &= \tilde{\Omega}_{mn} \tilde{\Omega}_{nm}, \\ T_{ij}^{(3)} &= \tilde{S}_{ik} \tilde{S}_{kj} - \frac{1}{3} \delta_{ij} \tilde{S}_{mn} \tilde{S}_{nm}. \end{aligned}$$

To model $\hat{\mathbf{R}}$ we assume that it takes the form

$$\hat{\mathbf{R}} = 2k \frac{\partial U_i}{\partial x_j} b_{ij}^R,$$

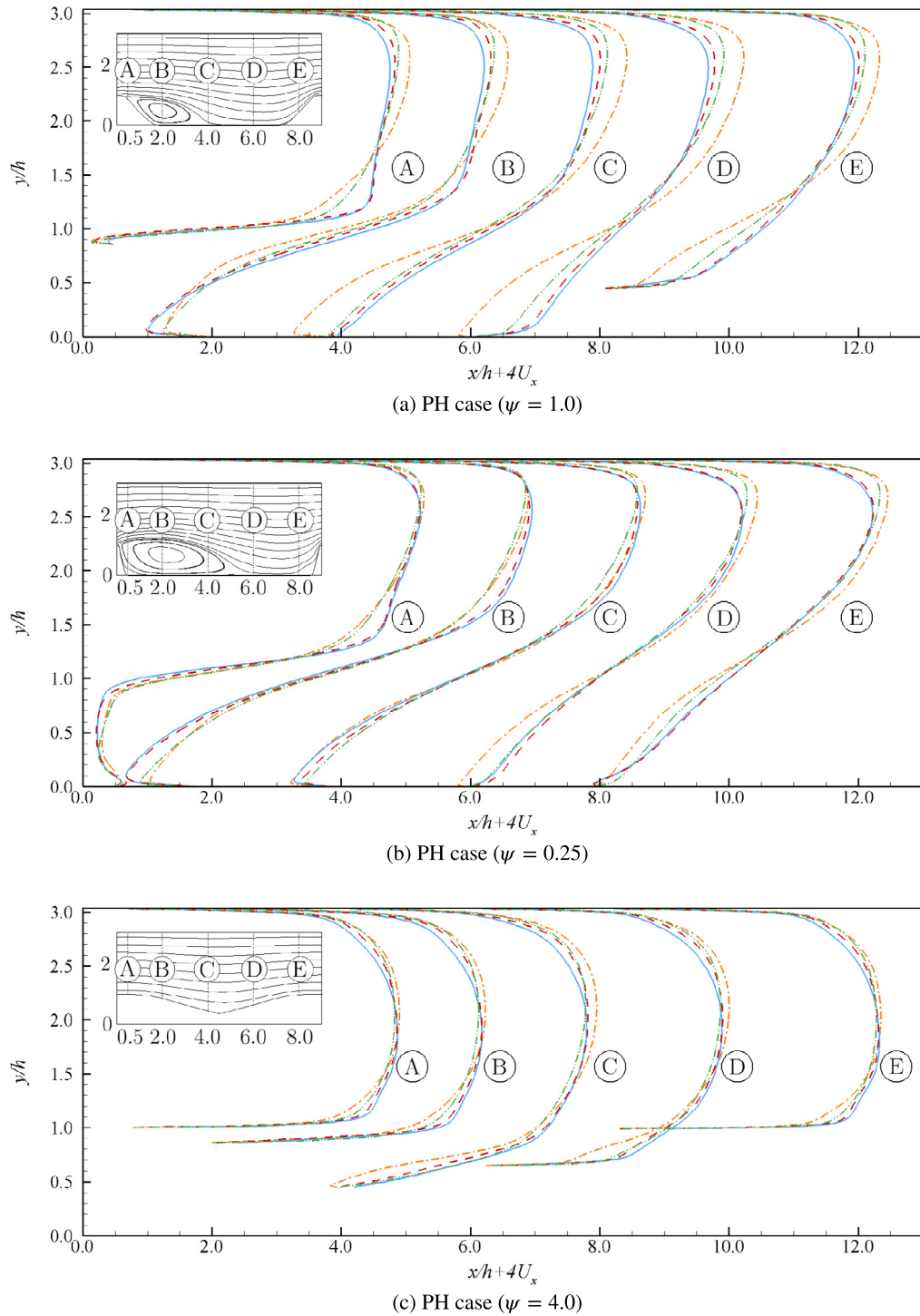


Fig. 2. Mean velocity profiles for PH cases: reference LES (—) (INCA), Frozen RANS (---), SpARtA RANS (-.-.-) and RANS with $k-\omega$ SST turbulence modelling (.....).

for some tensor-field b_{ij}^R , modelled similarly to b_{ij}^A by (7). It remains to fit a function of the form (7) to the LES data, for which we use symbolic regression.

For details refer to Schmelzer et al. [33]. In short, we form a large *library* of candidate basis functions, consisting of powers and products of the invariants λ_m . We then regress the data – consisting of $(\lambda_m, T_{ij}^{(n)}, b_{ij}^A)$ triples at each spatial

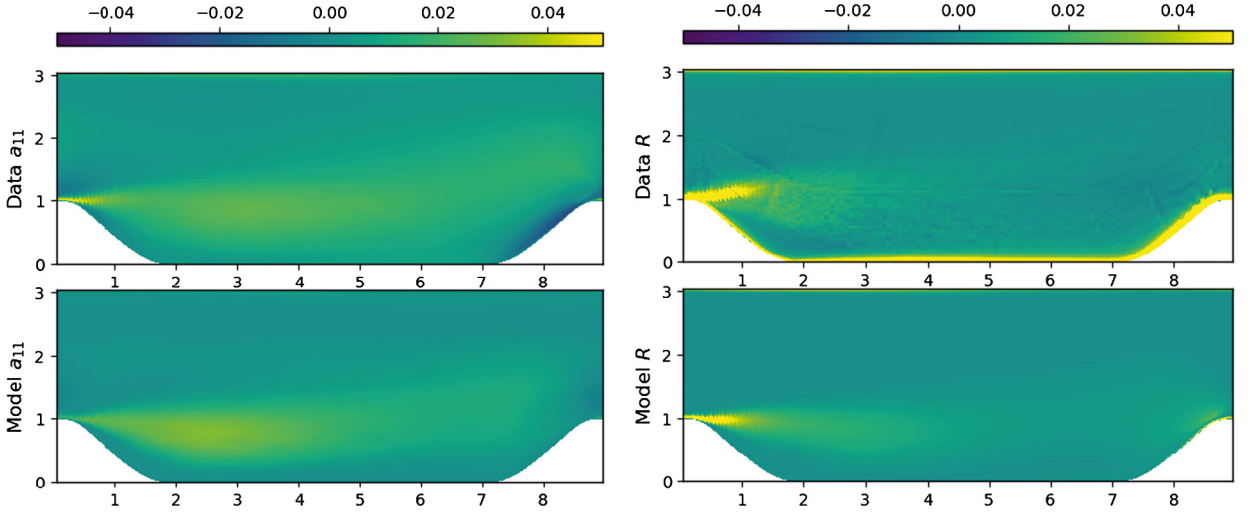


Fig. 3. Comparison of exact corrective field (based on LES) and SpaRTA model prediction (left: a_{11} in Reynolds stress; Right: R residual of k transport equation).

mesh point – against this library with sparsity-promoting ℓ^1 regularization. This selects a small set of basis functions that represent the data well. Concretely, let the regressing function be:

$$b_{ij}^{\Delta} \simeq \sum_{n=1}^4 T_{ij}^{(n)} \left\{ \sum_{m=1}^M \phi_m(\boldsymbol{\lambda}) \cdot \theta_n^m \right\} = L(\mathbf{T}, \boldsymbol{\lambda}; \boldsymbol{\theta}),$$

where $\boldsymbol{\theta}$ are coefficients of the M basis functions in the library $\phi_m(\cdot)$ for each basis tensor, and $L(\cdot)$ is the implied operator, which is linear in $\boldsymbol{\theta}$. Then we solve the elastic-net regularized regression problem:

$$\boldsymbol{\theta}_{\text{fit}} := \arg \max_{\boldsymbol{\theta} \in \Theta} \left\| L(\mathbf{T}^*, \boldsymbol{\lambda}^*; \boldsymbol{\theta}) - b_{ij}^{\Delta} \right\|_2^2 + \sigma \rho \|\boldsymbol{\theta}\|_1 + \sigma(1 - \rho) \|\boldsymbol{\theta}\|_2^2, \quad (8)$$

where the first norm is over all mesh points of all training cases, and once again \star denotes quantities evaluated from the LES data. We solve for a number of different values of σ and ρ , to obtain a number of candidate sparsity patterns, and we discard the values of the nonzero coefficients $\boldsymbol{\theta}$. For each of the sparsity patterns, we perform ridge regression, using only the basis functions identified in the sparse regression. Let $\boldsymbol{\theta}^s$ be a vector of non-zero coefficients identified by (8), then we solve

$$\boldsymbol{\theta}_{\text{fit}}^s := \arg \max_{\boldsymbol{\theta} \in \Theta} \left\| L(\mathbf{T}^*, \boldsymbol{\lambda}^*; \boldsymbol{\theta}^s) - b_{ij}^{\Delta} \right\|_2^2 + \sigma_r \|\boldsymbol{\theta}^s\|_2^2, \quad (9)$$

for each sparsity pattern. The final model is selected based on a compromise between sparsity, goodness-of-fit, and ideally performance in cross-validation if data is available (Schmelzer et al. [33]). This two step procedure allows us to independently control the level of sparsity (with ρ , σ), and the magnitude of the resulting coefficients (with σ_r), which can otherwise become very large.

Applying this procedure to our LES data for the standard P-H case ($\psi = 1$), the resulting algebraic models for b_{ij}^{Δ} and $\hat{\mathbf{R}}$ are:

$$b_{ij}^{\Delta} \simeq M_{b_{ij}^{\Delta}} = 2.8T_{ij}^{(2)}; \quad \hat{\mathbf{R}} \simeq M_{\mathbf{R}} = 0.4T_{ij}^{(1)} \cdot 2k \frac{\partial U_i}{\partial x_j}. \quad (10)$$

Fig. 3 shows the optimal $a_{ij} = 2kb_{ij}^{\Delta}$ and $\hat{\mathbf{R}}$ identified for the P-H case using the k -frozen approach of the previous section. The predictions of the model (10) are also shown. The agreement is generally good, with the notable exception of the large $\hat{\mathbf{R}}$ near the wall, which is not reproduced by (10). This failure can be attributed to the non-dimensionalization of S , Ω by the specific dissipation rate ω , which becomes large close to the wall, pulling all basis-tensors $T^{(n)}$ down to zero. This effect can be overcome by using coefficients α_n that go to infinity near the wall, as in Kaandorp and Dwight [22]. However, we consider this unnecessary, as corrections close to the wall, especially in b^{Δ} , have very little effect on the mean-flow.

Note that the above regression procedure is independent of the CFD solver, and is performed on a mesh-point-wise basis with flat data-vectors. Once the resulting SpaRTA model is obtained, it is implemented as an OpenFOAM turbulence model module in C++ using automatic code generation. The module is compiled, and dynamically linked to the main solver, without the need for recompiling OpenFOAM itself.

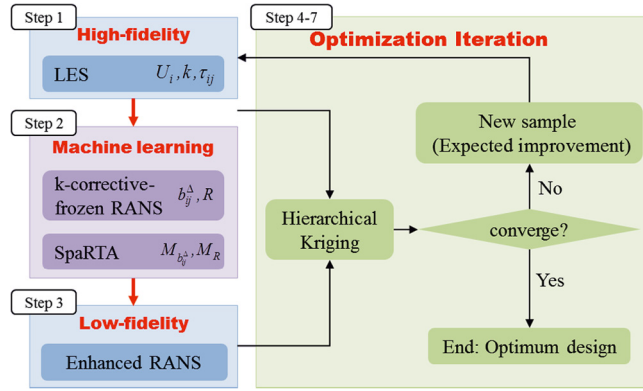


Fig. 4. Flowchart of the adaptive variable-fidelity optimization.

Having implemented $M_{b_{ij}^\Delta}$ and $\hat{\mathbf{R}}$ in the RANS solver, we verify that the mean-flow of the training case is reproduced, and we make predictions for $\psi = 0.25$ and $\psi = 4.0$ and compare with our LES reference, see Fig. 2. In all cases the mean-flow is significantly improved over the baseline $k-\omega$ SST, but do not always reach the accuracy of the directly injected corrective fields shown (“frozen RANS” in Fig. 2) which represent a best case scenario.

4. Bi-fidelity optimization loop with custom RANS as low-fidelity

We aim to efficiently solve the discretized PDE-constrained minimization problem

$$\min_{\psi \in \Psi} J(\psi; U) \quad \text{subject to} \quad R_{\text{LES}}(\psi; U) = 0,$$

where ψ are geometric design-variables in the design space Ψ , U is the full flow-state, J is the cost-function and R_{LES} is the (highest-fidelity) discretized PDE operator (which depends on ψ via boundary-conditions). We assume that no significant modelling is required to evaluate J given U , which is the case for most cost-functions of interest. We also have available a low-fidelity discretized operator $R_{\text{RANS}}[M](\psi; U)$, which depends on some closure model M derived using the procedure of the previous section.

The outline of our proposed bi-fidelity optimization is given in Fig. 4. The steps are:

1. Solve $R_{\text{LES}}(\psi_0, U) = 0$ for the baseline geometry $\psi = \psi_0$, to obtain turbulence statistics U^* , τ_{ij}^* , k^* . Let $i = 0$.
2. Identify the model-form error terms b_{ij}^Δ and $\hat{\mathbf{R}}$ using the k -corrective-frozen-RANS approach of Section 3.1 and the LES data from Step 1. Subsequently find the algebraic models $M_{b_{ij}^\Delta}^0$, M_R^0 using Section 3.2, to obtain $R_{\text{RANS}}[M^0](\psi; U)$.
3. Generate $N \gg 1$ low-fidelity sample points ψ'_1, \dots, ψ'_N by design of experiment (DoE) (e.g. Latin-hypercube sampling) in the (possibly multi-dimensional) design space. Solve $R_{\text{RANS}}[M^i](\psi'_j; U) = 0$ and evaluate J at each sample $j \in \{1, \dots, N\}$.
4. Build a bi-fidelity Kriging surrogate of J using LES samples at ψ_1, \dots, ψ_i , and low-fidelity samples at ψ'_1, \dots, ψ'_N .
5. Choose new high-fidelity sample ψ_{i+1} by maximum expected improvement on the surrogate of Step 4. Evaluate LES at this point.
6. Train a new low-fidelity model M^{i+1} based on LES data at $\psi_1, \dots, \psi_{i+1}$.
7. $i \leftarrow i + 1$. If convergence is achieved, then terminate; otherwise goto Step 3.

Note that in this work the low-fidelity model depends on the result of the high-fidelity (and the locations at which this is evaluated), in contrast to standard multi-fidelity models. This presents a challenge from the standpoint of statistical modelling of the bi-fidelity system – for example in co-Kriging, where a prior correlation relationship must be specified between the fidelities. This will be the subject of future work. We bypass the issue here by using hierarchical Kriging. The optimization algorithm is conducted using an in-house tool “SurroOpt” (Han [11]). Note that our methodology is independent of the LES mesh-resolution, and can be combined with any other high-fidelity data source, such as DES or DNS. Our surrogate based optimization framework already generalizes to high-dimensional parameter spaces, constraints, and multiple objectives, see Appendix A.

4.1. Variable-fidelity surrogate modelling: hierarchical Kriging

The hierarchical Kriging model (Han and Görtz [13]) (HK) is constructed in a recursive way. First, an ordinary Kriging model \hat{J}_{Low} is built for the low-fidelity objective function. Then a surrogate for the high-fidelity cost function \hat{J} is built

using the scaled low-fidelity Kriging model \hat{J}_{Low} as the model trend. In this way the high-fidelity responses are treated as realizations of a random process:

$$\hat{J}(\psi) = \rho \hat{J}_{\text{Low}} + Z(\psi) \quad (11)$$

where Z is a stationary Gaussian process with zero mean and a covariance $\text{Cov}[Z(\psi), Z(\psi^*)] = \sigma^2 r(\psi, \psi^*)$, where σ^2 is the process variance, and $r(\cdot, \cdot)$ and the correlation function. In this paper, we use a cubic spline function (Han and Görtz [13]), which introduces hyper-parameters θ .

Similar to the standard single-fidelity Kriging model, the corresponding predictor and mean-squared error (MSE) of Kriging for the high-fidelity cost function are

$$\hat{J}(\psi) = \rho \hat{J}_{\text{Low}}(\psi) + \mathbf{r}^T \mathbf{R}^{-1} (\mathbf{J} - \rho \mathbf{F}) \quad (12)$$

$$\varepsilon(\psi)^2 = \sigma^2 \{1 - \mathbf{r}^T \mathbf{R}^{-1} \mathbf{r} + [\mathbf{r}^T \mathbf{R}^{-1} \mathbf{F} - \hat{J}_{\text{Low}}(\psi)]^2 / (\mathbf{F}^T \mathbf{R}^{-1} \mathbf{F})^{-1}\} \quad (13)$$

where

$$\mathbf{F} = [\hat{J}_{\text{Low}}(\psi_1), \dots, \hat{J}_{\text{Low}}(\psi_N)] \in \mathbb{R}^N.$$

Here, $\mathbf{J} \in \mathbb{R}^N$ is the vector of high-fidelity observations at sample sites $\psi = [\psi_1, \dots, \psi_N]$. \mathbf{R} is the correlation matrix between the observed high-fidelity samples and \mathbf{r} is the correlation vector between the observed samples and the predicting point. Therefore, the Kriging model for high fidelity cost function can be regarded as a sum of scaled lower fidelity Kriging predictor and the discrepancy between the scaled lower-fidelity function and higher-fidelity function.

Model fitting of the HK model uses the maximum-likelihood estimate:

$$\max_{\rho, \theta, \sigma^2} L(\rho, \theta, \sigma^2) = \max_{\rho, \theta, \sigma^2} \frac{1}{\sqrt{2\pi\sigma^2|\mathbf{R}|}} \exp \left[-\frac{1}{2} \frac{(\mathbf{J} - \mathbf{F}\rho)^T \mathbf{R}^{-1} (\mathbf{J} - \mathbf{F}\rho)}{\sigma^2} \right], \quad (14)$$

given which an explicit expression for ρ is:

$$\rho = (\mathbf{F}^T \mathbf{R}^{-1} \mathbf{F})^{-1} (\mathbf{F}^T \mathbf{R}^{-1} \mathbf{J}).$$

It remains to specify in what manner new high-fidelity samples are chosen. We use the maximum expected improvement (EI) principle (Jones et al. [20], Zhang et al. [39]). Define the *improvement* with respect to a current best value J_{\min} as (formally):

$$I(\psi) = \max(J_{\min} - \hat{J}(\psi), 0).$$

Since the prediction of the HK model at any untried site ψ is the normal distribution $\mathcal{N}(\hat{J}(\psi), \varepsilon(\psi)^2)$, we choose the value of ψ that maximizes the expected improvement $\mathbb{E}I(\psi)$. This has a closed form expression:

$$\mathbb{E}I(\psi) = (J_{\min} - \hat{J}(\psi)) \Phi \left(\frac{J_{\min} - \hat{J}(\psi)}{\varepsilon(\psi)} \right) + \varepsilon(\psi) \phi \left(\frac{J_{\min} - \hat{J}(\psi)}{\varepsilon(\psi)} \right),$$

where $\phi(\cdot)$ and $\Phi(\cdot)$ are respectively the unit normal density and distribution functions.

4.2. Periodic hill optimization: cost function and design-space exploration

The baseline periodic-hill geometry (hill width $\psi = 1$) is the widely known ERCOFTAC Testcase 9.2 with the geometry definition of Mellen et al. [25]. The design variable is the normalized hill width: we simply scale the geometry of the original hill as $(x, y, z) \rightarrow (\psi * x, y, z)$, as illustrated in Fig. 5, while holding constant the distance between subsequent peaks. For very wide hills (e.g. $\psi = 4$) the hills overlap, and no flat region between the hills remains. The geometries of periodic-hills at the lower- and upper-boundary of the design-space are shown in Fig. 5.

We choose an cost function depending on the total drag on the hills and averaged turbulence kinetic energy over the whole flow field (at a constant mass-flow). The objective is to search for the geometry with maximum turbulence kinetic energy and minimum drag. A typical engineering application with similar objectives is the design of reactors or heat exchangers in process engineering, where one tries to minimize pressure loss and maximize turbulent mixing of reactants or of hot- and cold fluids. For the present proof-of-concept optimization, weights for these two terms such that the global optimum is not too close to the upper and lower boundaries of the design-space $\Psi = [0.25, 4]$. This choice allows us to demonstrate unconstrained optimization in this proof-of-concept study. The chosen function is:

$$\min_{\psi \in \Psi} \underbrace{-(\bar{k} - 2.5f)/J_0}_J, \quad \Psi = [0.25, 4] \quad (15)$$

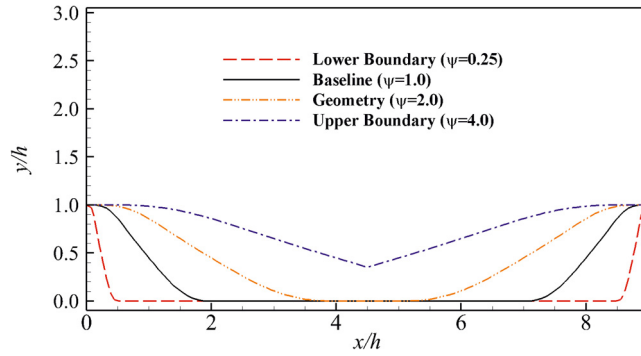


Fig. 5. Geometry illustrations for the design space.

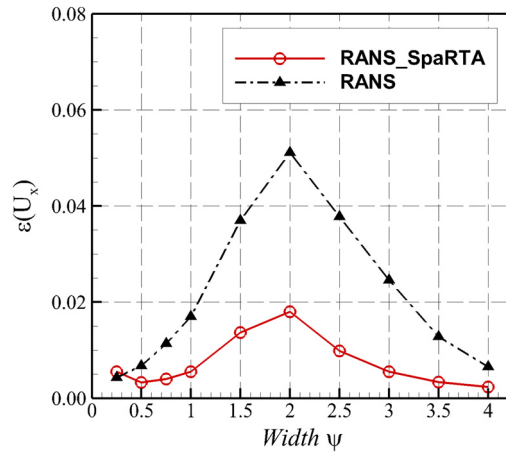


Fig. 6. Mean-squared error of mean velocity obtained by custom RANS and baseline RANS.

where \bar{k} , is the averaged turbulent kinetic energy over the flowfield, and f , the volume forcing term in (1), acts as a proxy for drag. The cost function J is normalized by the LES result of the baseline geometry, $J_0 := \bar{k}^* - 2.5 f^*$.

No validation data exists for these geometries, so our confidence in the correctness of our LES rests on the validation we performed for the standard geometry in Section 2.2. Note that in this work, LES is used as our ground-truth: the target of our optimization is the LES optimum. As such it's accuracy is not of primary concern for validating our method, provided only that it's significantly more accurate than baseline RANS.

Before the optimization we explore the design space with the reference LES, and the baseline- and customized RANS models. We use the custom model (10) trained at $\psi = 1$ from Section 3.2 and compare against our LES ground-truth.

In Fig. 6, we see that the mean-velocity prediction is significantly improved compared with the baseline RANS simulation, across the majority of the design-space. Fig. 7 shows that the prediction of the averaged turbulence kinetic energy \bar{k} and proxy-drag f are both significantly improved - a consequence of more accurate Reynolds stresses and mean flow fields for all test geometries. The custom RANS performs best when $\psi \geq 1$, for which the flow shows a medium-sized separation bubble. For the steeper geometries $\psi < 1$, the larger separation bubbles are slightly under-estimated by the custom closure model. In Fig. 8, we observe that the custom RANS matches the main trend of the LES objective function very well. The LES optimization problem has two local minima, near $\psi = 0.75$ and $\psi = 2.0$, whereas the objective estimated by the custom RANS only shows the first. With additional hi-fidelity LES samples, the custom RANS model becomes more accurate as the optimization progresses. The baseline RANS model, however, does not reproduce the magnitude of the objective function, nor the general location of the minima: a consequence of significantly under-predicting both drag and Reynolds stress.

Despite the simple geometry, this flow is governed by highly complex interactions between mean flow acceleration and deceleration, separation on a curved wall, turbulent mixing in the separated shear layer, flow reattachment and redevelopment of the boundary layer. The relation between the design variable ψ , turbulence kinetic energy and pressure drag is therefore nonlinear and non-monotonic, which leads to two minima with the chosen objective function. We don't have a detailed physical explanation for this phenomena, nor the kink near $\psi = 0.7$ (visible in Fig. 9). This could be the subject of a further paper looking at the detailed flow-physics of this parameterized geometry.

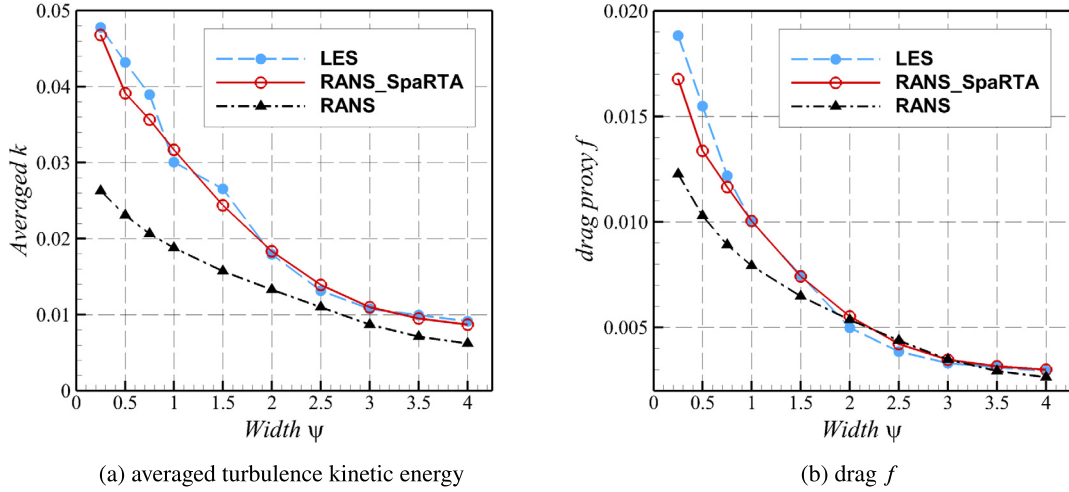


Fig. 7. Comparison of cost-function components obtained by LES, custom RANS and baseline RANS.

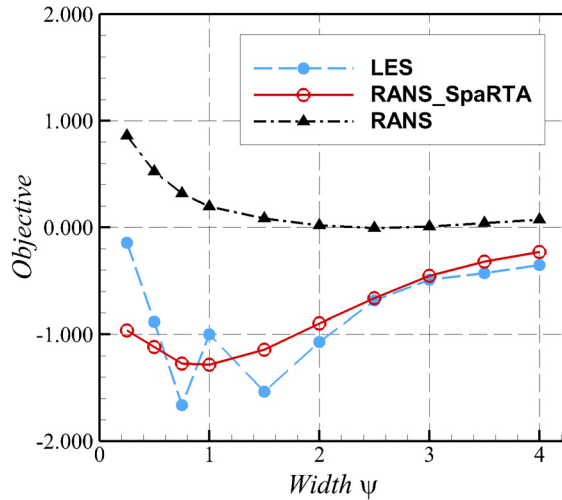


Fig. 8. Design-space exploration of the objective function J .

4.3. Optimization convergence

Our expectation is that: by enhancing quality of the low-fidelity model, the convergence of the bi-fidelity optimization will be improved. The low-fidelity model need not be highly-accurate for the whole design space in order to be useful. Indeed given a single LES training sample, we expect the customized-RANS closure to be most accurate close to the training point, and least accurate at the limits of the design space. As the optimization progresses, and more LES samples are added, we then expect to become more accurate wherever there are LES samples.

The optimization starts, as shown in Fig. 9(a), with one LES as the high-fidelity sample (red solid circles) and 26 custom RANS simulations as the low-fidelity samples (red hollow circles). The initial HK response surface passes through the LES, and since there is only a single high-fidelity sample, the shape is dictated entirely by the custom RANS, and the scaling parameter ρ in HK model is found to be 0.78. The expected improvement criterion selects a second LES sample at $\psi \simeq 0.93$, Fig. 9(a). LES is performed at this point, and a custom closure is built, which is found to be $b_{ij}^\Delta \simeq M_{b_{ij}^\Delta} = 1.2T_{ij}^{(2)}$, and $\hat{\mathbf{R}} \simeq M_R = 0.45T_{ij}^{(1)} \frac{\partial U_i}{\partial x_j}$. Using this new closure model, the low-fidelity samples everywhere in the design space are reevaluated. With the updated low-fidelity samples and two LES high-fidelity samples, the HK model is rebuilt, shown in Fig. 9(b). Again the closure passes through the LES samples exactly, and the hierarchical Kriging is closer to the true cost function in the region near the optimum. The scaling parameter ρ in the HK model is found to be 0.93, closer to 1 because of the better match between low- and high-fidelity objective functions. A third iteration is shown in Fig. 9(c). The convergence of the procedure in terms of J is shown in Fig. 10 (red solid line). In Fig. 9, the reference for the objective function is obtained by performing 59 LES samples in the design space (Fatou Gómez [8]).

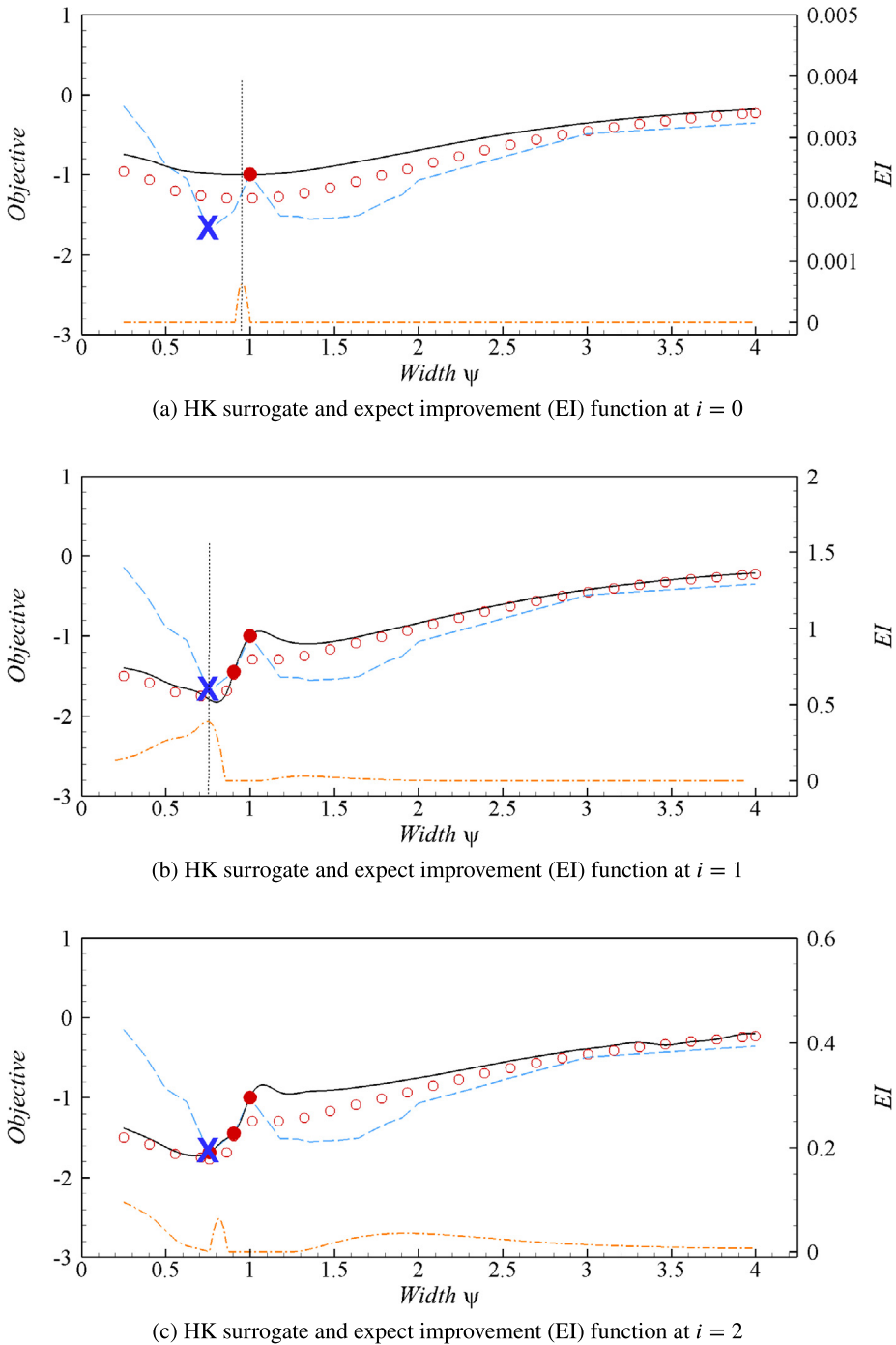


Fig. 9. Three iterations of the proposed method. (reference by LES (- - -) (Fatou Gómez [8]), HK (-), EI (- - -), hi-fidelity LES samples (•), low-fidelity custom RANS (◦) and global optimum (X)).

Note that in Fig. 9 the initial values of the EI peak are very low, and at later iterations higher. This is fairly typical behavior for the EI in Kriging-based optimization; a consequence of initial poor estimation of the Kriging hyper-parameters by maximum-likelihood estimation (MLE), due to the very low number of samples. The variance of the Kriging model (as well as the length-scale) changes significantly as each new sample is added, leading to large changes in both the response, and especially the EI. This problem reduces as the number of samples increases, and disappears in the limit. Given that we are using very few samples, an alternative to MLE is to specify variance and length-scales by hand and keep them fixed.

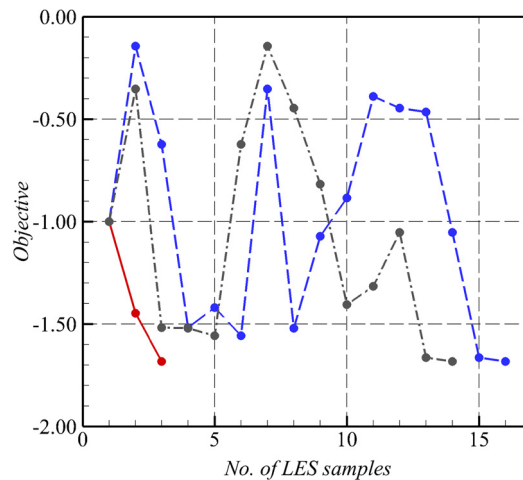


Fig. 10. Convergence of bi-fidelity optimization (custom RANS as low-fidelity model (—, •), baseline RANS as low-fidelity model (- - -, •), and single fidelity optimization using LES only (- · - ·, •).

This has the disadvantage of adding more parameters to the method, and potentially biasing the EI however, so we do not use it here.

As a comparison, we also performed a single-fidelity optimization using only the high-fidelity LES model, and a bi-fidelity optimization using the baseline RANS as the low-fidelity model. With the same initial LES sample, the convergence histories in terms of J are shown in Fig. 10 (black dash-dotted line and blue dashed line, respectively), where in each case we show the objective-function value of the most recently obtained sample. The convergence history of bi-fidelity optimization using the baseline RANS model as the lo-fi model, shows no improvement over the single-fidelity optimization – and is in fact significantly more expensive than pure LES optimization, due to the large number of additional RANS solves needed. This is a typical example bi-fidelity methods with poor lo-fi to hi-fi correction resulting in no speed-up compared to hi-fi only. Consequently, more than 10 LES samples are required to locate the global optimum.

The convergence criterion used in these optimizations, simply detects when J achieves the global optimum based on the 59 reference LES simulations. This is not practical in real applications, where we would suggest using one of the standard EGO-based convergence criteria.

Finally, the optimum solution is found at $\psi = 0.75944$ with the cost function value around -1.68 . In summary, the optimization with our proposed methodology converged to within the accuracy of the high-fidelity model with only 2 LES samples, with one further sample used to verify the result.

5. Conclusions

In this work, a novel bi-fidelity fluid-dynamic shape optimization methodology is proposed, in which LES is used as the high-fidelity simulation tool and an automatically customized RANS turbulence closure as the low-fidelity model. The full-field LES data obtained from the high-fidelity samples are used to train a RANS model for the flow being optimized. The SpARTA method is used as a robust and effective way of tailoring RANS models with simple algebraic augmentation. The customized low-fidelity RANS model is successively improved as more LES data becomes available within the design space. The two fidelities are combined in a hierarchical Kriging surrogate, and the EGO procedure is used to add new high-fidelity samples.

Given the technical complexity of this procedure, we have demonstrated it on a proof-of-concept shape optimization of a periodic-hill geometry with varying hill-width. In this case, the method converges to the true optimum (within the tolerance of the LES simulations) in two iterations. Shape optimization for flow-problems where the details of turbulence are important, including separated flows, junction flows, and transitional flows, may become computationally feasible with this scheme. Our methodology is independent of LES resolution (e.g. wall-resolved LES could be used without modification), and could be combined with any other reference method, URANS, DES, DNS etc.

Future work will target application to a three-dimensional optimization problem of engineering interest. Our goal is that this will serve as a demonstrator of LES-driven optimization as a serious option in engineering optimization. Such a problem will likely involve high-dimensional parameter spaces, constraints, and possibly multiple objectives. The surrogate-based optimization we use here, generalizes well to all these requirements, see Appendix A, and will not be the bottleneck. It remains to be seen whether our customized RANS models will generalize well within more general parameter-spaces, and how they will cope with design-spaces incorporating dramatically different physics at different design points.

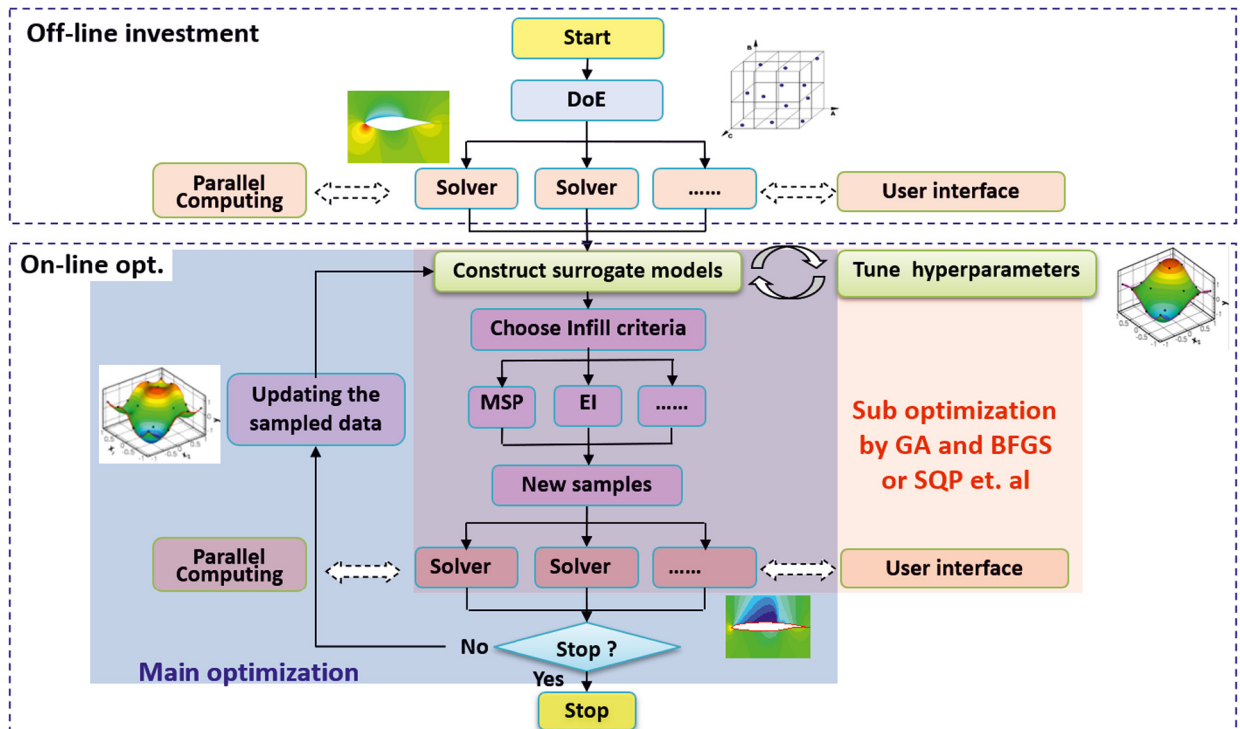


Fig. 11. Flowchart of a SBO-type optimizer SurroOpt.

Declaration of competing interest

The authors declare that they have no known competing financial interests or personal relationships that could have appeared to influence the work reported in this paper.

Appendix A. Surrogate based optimization with SurroOpt

SurroOpt (Han [11]) is a research code developed for academic- and engineering design driven by expensive numerical simulations. It is a surrogate-based optimization (SBO) code, which can be used to efficiently solve arbitrary single and multi-objective (Pareto front), unconstrained and constrained optimization problems in high-dimensional parameter spaces (Fig. 11).

Generally, a SBO process consists of the following steps:

1. Initial sample points are chosen by a *design of experiment* (DoE) method, and the objective(s) and constraints are evaluated at the samples by an expensive numerical analysis code such as CFD solver.
2. Initial surrogate models for the objectives and constraints are built, based on the sampling dataset.
3. A sub-optimization solves an optimal infill-sampling problem, based on the models from step 2., which in turn generates new sample points to be evaluated by the expensive analysis code.
4. The newly selected sample points, as well as the functional responses are added to the sample database and the surrogate models are updated.
5. Steps 3. and 4. are repeated until a termination condition is satisfied.

The main ingredients of such a SBO process are therefore: DoE, surrogate modeling, infill-sampling and sub-optimization, and termination conditions. SurroOpt has built-in modern DoE methods suited for deterministic computer experiments, such as Latin hypercube sampling (LHS), uniform design (UD) and Monte Carlo design (MC). A variety of surrogate models are included, such as quadratic response surface models (PRSM), kriging, gradient-enhanced kriging (GEK), hierarchical kriging (HK), co-Kriging, radial-basis functions (RBFs), artificial neural network (ANN), support-vector regression (SVR), etc. A number of infill-sampling criteria and the dedicated constraint handling methods are available, such as minimizing surrogate prediction (MSP), minimizing lower confidence bounding (LCB), maximizing expected improvement (EI), maximizing probability of improvement (PI), and maximizing mean squared error (MSE). Some well-known optimization algorithms, such as Hooke & Jeeves pattern search, BFGS quasi-Newton method, sequential quadratic programming (SQP), or single/multi objective GAs, are employed to solve the sub-optimizations, in which the cost function(s) and constraint function(s) are evaluated

by the cheap-to-evaluate surrogate models. In turn, new sample points are generated and evaluated by the expensive analysis code. Four termination conditions are defined in `SurroOpt`, which set thresholds for the maximum number of CFD evaluations, the minimum distance between samples, the minimum value of expected improvement or the accuracy of surrogate model. `SurroOpt` manages compute cores with MPI, giving the user several options for parallelization of the simulation code and sampling strategy. See (Han [11]) for details and references.

This framework will allow us to generalize the methodology described in this paper to high-dimensional, multi-objective, constrained optimization problems of practical engineering interest.

References

- [1] G. Almeida, D. Durao, M. Heitor, Wake flows behind two-dimensional model hills, *Exp. Therm. Fluid Sci.* 7 (1993) 87–101, [https://doi.org/10.1016/0894-1777\(93\)90083-U](https://doi.org/10.1016/0894-1777(93)90083-U).
- [2] Z. Belligoli, A.J. Koers, R.P. Dwight, G. Eitelberg, Using an anti-fairing to reduce drag at wing/body junctions, *AIAA J.* 57 (2019) 1468–1480, <https://doi.org/10.2514/1.J057481>.
- [3] M. Breuer, N. Peller, C. Rapp, M. Manhart, Flow over periodic hills – numerical and experimental study in a wide range of Reynolds numbers, *Comput. Fluids* 38 (2009) 433–457, <https://doi.org/10.1016/j.compfluid.2008.05.002>.
- [4] K.J. Chang, R.T. Haftka, G.L. Giles, P.J. Kao, Sensitivity-based scaling for approximation structural response, *J. Aircr.* 30 (1993) 283–288.
- [5] Z. Chen, S. Hickel, A. Devesa, J. Berland, N. Adams, Wall modeling for implicit large-eddy simulation and immersed-interface methods, *Theor. Comput. Fluid Dyn.* 28 (2014) 1–21.
- [6] K. Duraisamy, G. Iaccarino, H. Xiao, Turbulence modeling in the age of data, *Annu. Rev. Fluid Mech.* 51 (2019) 357–377, <https://doi.org/10.1146/annurev-fluid-010518-040547>.
- [7] P.A. Durbin, Some recent developments in turbulence closure modeling, *Annu. Rev. Fluid Mech.* 50 (2018) 77–103, <https://doi.org/10.1146/annurev-fluid-122316-045020>.
- [8] J. Fatou Gómez, Multi-fidelity Co-Kriging optimization using hybrid injected RANS and LES, MSc Thesis, Delft University of Technology, 2018.
- [9] S.E. Gano, J.E. Renaud, B. Sanders, Hybrid variable fidelity optimization by using a Kriging-based scaling function, *AIAA J.* 43 (2005) 2422–2430.
- [10] R. Haftka, Combining global and local approximations, *AIAA J.* 29 (1991) 1523–1525, <https://doi.org/10.2514/3.10768>.
- [11] Z. Han, `SurroOpt` a generic surrogate-based optimization code for aerodynamic and multidisciplinary design, in: 30th Congress of the International Council of the Aeronautical Sciences, Daejeon, South Korea, 2016.
- [12] Z. Han, C. Xu, L. Zhang, Y. Zhang, K. Zhang, W. Song, Efficient aerodynamic shape optimization using variable-fidelity surrogate models and multilevel computational grids, *Chin. J. Aeronaut.* 33 (2020) 31–473, <https://doi.org/10.1016/j.cja.2019.05.001>.
- [13] Z.H. Han, S. Görtz, Hierarchical kriging model for variable-fidelity surrogate modeling, *AIAA J.* 50 (2012) 1885–1896, <https://doi.org/10.2514/1.J051354>.
- [14] Z.H. Han, S. Görtz, R. Zimmermann, Improving variable-fidelity surrogate modeling via gradient-enhanced kriging and a generalized hybrid bridge function, *Aerosp. Sci. Technol.* 25 (2013) 177–189.
- [15] Z.H. Han, R. Zimmermann, S. Görtz, Alternative cokriging model for variable-fidelity surrogate modeling, *AIAA J.* 50 (2012) 1205–1210, <https://doi.org/10.2514/1.J051243>.
- [16] S. Hickel, N. Adams, Efficient implementation of nonlinear deconvolution methods for implicit large-eddy simulation, in: *High Performance Computing in Science and Engineering*, vol. 6, 2007, pp. 293–306.
- [17] S. Hickel, N. Adams, J. Domaradzki, An adaptive local deconvolution method for implicit LES, *J. Comput. Phys.* 213 (2006) 413–436.
- [18] S. Hickel, T. Kempe, N.A. Adams, Implicit large-eddy simulation applied to turbulent channel flow with periodic constrictions, *Theor. Comput. Fluid Dyn.* 22 (2008) 227–242.
- [19] S. Hickel, E. Toubert, J. Bodart, J. Larsson, A parametrized non-equilibrium wall-model for large-eddy simulations, in: *Proceedings of the 2012 Summer Program, Center for Turbulence Research at Stanford University*, 2012, pp. 127–136.
- [20] D.R. Jones, M. Schonlau, W.J. Welch, Efficient global optimization of expensive black-box functions, *J. Glob. Optim.* 13 (1998) 455–492.
- [21] A.G. Journel, J.C. Huijbregts, *Mining Geostatistics*, Academic Press, 1978.
- [22] M.L. Kaandorp, R.P. Dwight, Data-driven modelling of the Reynolds stress tensor using random forests with invariance, *Comput. Fluids* 202 (2020) 104497, <https://doi.org/10.1016/j.compfluid.2020.104497>.
- [23] M.C. Kennedy, A. O'Hagan, Predicting the output from a complex computer code when fast approximations are available, *Biometrika* 87 (2000) 1–13, <https://doi.org/10.1093/biomet/87.1.1>.
- [24] J. Ling, A. Kurzawski, J. Templeton, Reynolds averaged turbulence modelling using deep neural networks with embedded invariance, *J. Fluid Mech.* 807 (2016) 155–166, <https://doi.org/10.1017/jfm.2016.615>.
- [25] C. Mellen, J. Fröhlich, W. Rodi, Large eddy simulation of the flow over periodic hills, in: *Proceedings of IMACS, World Congress, Lausanne*, 2000.
- [26] F.R. Menter, Two-equation eddy-viscosity turbulence models for engineering applications, *AIAA J.* 32 (1994) 1598–1605, <https://doi.org/10.2514/3.12149>.
- [27] M. Meyer, A. Devesa, S. Hickel, X.Y. Hu, N.A. Adams, A conservative immersed interface method for large-eddy simulation of incompressible flows, *J. Comput. Phys.* 229 (2010) 6300–6317.
- [28] M. Meyer, S. Hickel, C. Breitsamter, N.A. Adams, Wall-modelled implicit large-eddy simulation of the RA16SC1 highlift configuration, in: *31st AIAA Applied Aerodynamics Conference, AIAA paper 2013-3037*, American Institute of Aeronautics and Astronautics, San Diego, 2013.
- [29] E.J. Parish, K. Duraisamy, A paradigm for data-driven predictive modeling using field inversion and machine learning, *J. Comput. Phys.* 305 (2016) 758–774, <https://doi.org/10.1016/j.jcp.2015.11.012>.
- [30] S. Parneix, D. Laurence, P.A. Durbin, A procedure for using DNS databases, *J. Fluids Eng.* 120 (1998) 40–47, <https://doi.org/10.1115/1.2819658>.
- [31] S.B. Pope, A more general effective-viscosity hypothesis, *J. Fluid Mech.* 72 (1975) 331–340.
- [32] C. Rapp, Experimentelle studie der turbulenten Strömung über periodische Hügel, Ph.D. thesis, Technische Universität München, 2009.
- [33] M. Schmelzer, R.P. Dwight, P. Cinnella, Discovery of algebraic Reynolds-stress models using sparse symbolic regression, *Flow Turbul. Combust.* (2020), <https://doi.org/10.1007/s10494-019-00089-x>.
- [34] R.L. Simpson, Junction flows, *Annu. Rev. Fluid Mech.* 33 (2001) 415–443, <https://doi.org/10.1146/annurev.fluid.33.1.415>.
- [35] J.X. Wang, J. Wu, J. Ling, G. Iaccarino, H. Xiao, Physics-informed machine learning for predictive turbulence modeling: toward a complete framework, in: *Proceedings of the 2016 Summer Program, Center for Turbulence Research at Stanford University*, 2016, pp. 1–10.
- [36] J. Weatheritt, R. Sandberg, A novel evolutionary algorithm applied to algebraic modifications of the RANS stress-strain relationship, *J. Comput. Phys.* 325 (2016) 22–37, <https://doi.org/10.1016/j.jcp.2016.08.015>.

- [37] J. Weatheritt, R.D. Sandberg, The development of algebraic stress models using a novel evolutionary algorithm, *Int. J. Heat Fluid Flow* 68 (2017) 298–318, <https://doi.org/10.1016/j.ijheatfluidflow.2017.09.017>.
- [38] H. Xiao, P. Cinnella, Quantification of model uncertainty in RANS simulations: a review, *Prog. Aerosp. Sci.* 108 (2019) 1–31, <https://doi.org/10.1016/j.paerosci.2018.10.001>.
- [39] Y. Zhang, Z.h. Han, K.s. Zhang, Variable-fidelity expected improvement method for efficient global optimization of expensive functions, *Struct. Multi-discip. Optim.* 58 (2018) 1431–1451.